Express Polymer Letters Vol.17, No.6 (2023) 647–659
Available online at www.expresspolymlett.com
https://doi.org/10.3144/expresspolymlett.2023.47

Research article

Effect of loading strain rate on nano-indentation response of an aerospace grade epoxy polymer

Laura Alejandra Fasce[1,2*], *Lucas Sánchez Fellay*[1], *Patricia María Frontini*[1,3]

[1]Instituto de Investigaciones en Ciencia y Tecnología de Materiales (INTEMA), Universidad Nacional de Mar del Plata-CONICET, Av. C. Colón 10850, B7606WV Mar del Plata, Argentina
[2]Departamento de Ingeniería Química y en Alimentos, Facultad de Ingeniería, Universidad Nacional de Mar del Plata, Av. J. B. Justo 4302, B7608FDQ Mar del Plata, Argentina
[3]Departamento de Ingeniería en Materiales, Facultad de Ingeniería, Universidad Nacional de Mar del Plata, Av. J. B. Justo 4302, B7608FDQ Mar del Plata, Argentina

Received 23 September 2022; accepted in revised form 20 January 2023

Abstract. Depth sensing indentation holds the promise of local mechanical properties determination. However, the number of studies on materials that exhibit time-dependent and hydrostatic pressure-dependent behavior is still scarce. This paper aims to understand the effect of loading strain rate on the nano-indentation response of an aerospace epoxy resin by combining physical measurements and numerical simulations. Physical nano-indentation tests were carried out using a Berkovich indenter at different constant loading strain rates (0.01 to 1.25 s^{-1}). It was observed that as the loading strain rate increases, the penetration displacement at which the target load is reached decreases while the maximum displacement attained at the end of the load-hold period increases. The indentation response was numerically simulated to get insight into the phenomenon by finite element analysis. The polymer behavior was described by a nine-parameter elastic-viscoplastic constitutive model (EVP-9). Constitutive parameters were calibrated from uniaxial tensile and compression experimental data. Simulations agreed reasonably well with physical experiments being able to reproduce the loading strain rate effect observed in physical nano-indentation tests.

Keywords: *thermosetting resins, material testing, nano-indentation, mechanical properties, modelling and simulation*

1. Introduction

Nowadays, polymers play an important role in the development of thin coatings and bulk materials for high-performance applications in biomedical, aerospace, and automotive industries in which enhanced surface properties are required. This application demands appropriate surface mechanical characterization methods at micro and nano scales. Depth sensing indentation holds the promise of in situ estimation of surface mechanical properties from the measured force-penetration displacement (P–h) data. Knowledge of the influence of experimental conditions upon polymers' mechanical response and the development of proper methodologies are fundamental elements for the design of polymeric components.

RTM6 is a mono-component epoxy resin especially developed for the aerospace industry, and it is widely used as a matrix of composite materials. Surface mechanical properties characterization of similar grades of epoxy resins via nano-indentation experiments have been the focus of recent research [1–4]. Frontini *et al*. [4] explored the nano-indentation response of RTM6 at different strain rates and found inconsistent trends in mechanical properties – determined by the Oliver-Phar method – with strain rate.

*Corresponding author, e-mail: lfasce@fi.mdp.edu.ar

The Oliver-Pharr method [5] is suitable for elastoplastic solids but not for materials that exhibit time-dependent behavior, strain softening and hardening, and pressure dependency [6–8]. These polymer's mechanical characteristics cause the indentation elastic modulus and hardness values to depend on the applied contact conditions. Many efforts have been undertaken towards finding the proper testing conditions and procedure modifications to become the Oliver-Pharr analysis reliable for polymers [8, 9–12]. However, all these attempts are useful for material comparative purposes but do not capture the actual constitutive behavior of polymers [13].

The unambiguous identification of constitutive parameters from nano-indentation data is a challenging task that requires proper polymer's constitutive models [14–19], finite element modeling of the complex indentation problem, and inverse analysis methods [20]. The number of studies for materials that displays time and hydrostatic-dependent pressure-dependent behavior is still scarce [20–22]. Most of the studies deal with poly(methyl methacrylate) (PMMA) and polycarbonate (PC) materials [20–22]. Rueda-Ruiz *et al*. [20] proposed an inverse analysis approach to extract the elastoplastic properties from instrumented sharp micro-indentation in rate- and pressure-dependent materials and validated it for PMMA. However, neither viscoelastic effects nor strain-hardening effects were considered in the method [20]. van Breemer *et al*. [21] were capable to reproduce relatively well the micro-indentation and uniaxial compression responses of PMMA and PC using a twelve-parameter elastic-viscoplastic constitutive model. Anand and Ames [22] developed a more complex elastic-viscoplastic constitutive model that fitted quite well the micro-indentation response of PMMA using more than 30 parameters. Even though these works stated the basis for future constitutive parameter identification methods via inverse analysis for polymers, the authors remarked that a simplified constitutive model with a minimum number of essential parameters is still required [22].

In this work, a nine-parameter elastic-viscoplastic constitutive model (EVP-9) is chosen to describe the main features of RTM6 mechanical behavior. It belongs to a series of models that combine linear elastic springs, viscoplastic dashpots, and non-linear Langevin springs elements in parallel networks developed by Bergström [23]. These models have been widely adopted to simulate the mechanical response of several polymers under different test configurations, including indentation [14, 17, 18, 24–29]. To implement constitutive models that are not already available in finite element (FE) software, like ABAQUS, a user material subroutine (UMAT) is always required. In the case of the EVP-9 model, the UMAT can be easily implemented using the commercial PolyUMod application [23]. This software allows the user to build a constitutive model selecting the combination of elements -with different constitutive relationships- in parallel.

In this paper, the pronounced effect of loading strain rate on RTM6 indentation response is shown. Then, to give insight into the observed strain rate effects, FE numerical simulations are carried out considering the EVP-9 constitutive model calibrated using macroscale uniaxial stress-strain data.

2. Material and methods

2.1. Material and sample preparation

A commercial epoxy system utilized for resin transfer molding in the aerospace industry, RTM6 (HexFlow® RTM6, Hexcel Corporation, Stamford, USA), was used in this study. The RTM6 material block was prepared following the thermal cycle and procedure described by Morelle *et al*. in [30].

Nano-indentation specimens were prepared by polishing one face of the RTM6 block up to a surface roughness (R_a) lower than 1 nm was reached. The specimen looks like a yellow transparent prismatic block (2 mm thick).

2.2. Nano-indentation experiments

Physical nano-indentation experiments were performed in a Triboindenter (TI 750, Hysitron Inc., Minneapolis, USA) at room temperature using a diamond Berkovich tip and three-step load functions (loading/holding/unloading). No drift correction was applied to displacement data.

Tests were carried out at a constant indentation strain rate. For geometrically self-similar tips, indentation strain rate ($\dot{\varepsilon}$) is defined as [31–32] (Equation (1)):

$$\dot{\varepsilon} = \frac{\dot{h}}{h} \tag{1}$$

where $\dot{h}$ is the indenter displacement velocity, and h is the indenter penetration depth into the specimen. The loading force (P) was assumed to be related to $\dot{\varepsilon}$ and time (t) by [33] (Equation (2)):

$$P = P_0 e^{2\dot{\varepsilon}t} \quad (2)$$

where P_0 is the initial contact force (taken as 1 μN). Four different loading constant strain rates (*CSR*) were applied in the experiments ($\dot{\varepsilon}$ = 0.01, 0.05, 0.25, and 1.25 s^{-1}). The *CSR* range was selected according to the testing system's capability to acquire reliable data. The maximum *CSR* value was limited by the response capability of the equipment, while the minimum was by the influence of thermal drift errors in displacement signal for long time experiments. The minimum *CSR* value was chosen as the lowest value at which *P–h* curves appeared as reproducible as for the other *CSR* conditions.

In exploratory tests, the maximum applied load (P_{max}) was varied from 1500 to 6000 μN, holding time at maximum load (t_{hold}) was taken as 5 and 10 s, while unloading time (t_{unload}) was kept constant at 1 s. The following testing conditions were finally selected to analyze the effect of *CSR* on *P–h* curves: P_{max} = 6000 μN, t_{hold} = 10 s, and t_{unload} = 1 s. For each *CSR* condition, 16 indentations were conducted on the RTM6 specimen. No size-effects are expected at the penetration depths achieved in the experiments [34].

Plastic work values (W_p), *i.e.*, the energy spent in plastic deformation, were determined by integrating the loading and holding portion of *P–h* curves (total work done) and subtracting the area under the unloading portion (visco-elastic recovery).

Reduced elastic modulus (E_r) and indentation hardness (H) values were calculated following Oliver and Pharr approach [5]. This method assumes that the material behavior during unloading is elastic and proposes a power law fitting function for the unloading curve. The contact stiffness (S) is calculated as the slope of the unloading curve at the beginning of unloading, *i.e.*, at $h = h_{max}$ (h_{max} is the maximum indenter penetration depth into the specimen). The contact depth (h_c) is calculated as (Equation (3)):

$$h_c = h_{max} - \varepsilon \frac{P_{max}}{s} \quad (3)$$

where ε is a tip geometry factor equal to 0.75. E_r and H are calculated as (Equations (4) and (5)):

$$E_r = \frac{s\sqrt{\pi}}{2\sqrt{A_c}} \quad (4)$$

$$H = \frac{P_{max}}{A_c} \quad (5)$$

being A_c the actual contact area obtained from multiple indentations in a standard PC sample (Equation (6)):

$$A_c = 24.5h_c^2 + 2.88879 \cdot 10^3 h_c \quad (6)$$

2.3. EVP-9 material constitutive model

The constitutive model consists of three separate elements arranged in two networks (*A* and *B*) that act in parallel, as shown in Figure 1. The total Cauchy stress (T) and deformation gradient (F) are given by (Equations (7) and (8)):

$$T = T_A + T_B \quad (7)$$

$$F = F_A + F_B \quad (8)$$

Network A is composed of a linear elastic spring connected in series with a viscoplastic dashpot, while network B is made by a non-linear Langevin spring. The kinematic framework of the model is deeply described elsewhere [26], while the constitutive relationships between T and F are described below.

The stress acting on networks A and B are (Equations (9) and (10)):

$$T_A = \frac{1}{J}\mathfrak{d}^e\left[\ln U_A^e\right] \quad (9)$$

$$T_B = \frac{\mu}{J\bar{\lambda}} \frac{\mathfrak{d}^{-1}\frac{\bar{\lambda}}{\lambda_{lock}}}{\mathfrak{d}^{-1}\frac{1}{\lambda_{lock}}} \mathrm{dev}(B_b) \quad (10)$$

where $J = \det[U_A^e]$ and $\mathfrak{d}^e$ is a 4th-order tensor that contains elastic parameters (the Young modulus (E) and Poisson ratio (ν for isotropic materials, μ is the shear modulus, λ_{lock} is the locking stretch,

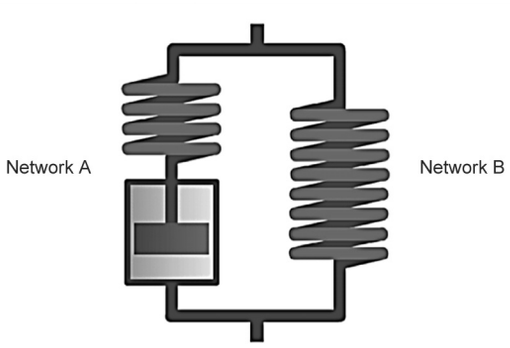

Figure 1. Rheological representation of elastic-viscoplastic EVP-9 constitutive model framework.

$B_B = J^{-2/3}FF^T$ the distortional part of the left Cauchy-Green tensor (Equation (11)):

$$\bar{\lambda} = \sqrt{\frac{\mathrm{tr}[B_B]}{3}} \tag{11}$$

$\vartheta^{-1}(x)$ the inverse Langevin function.

The plastic strain rate $\dot{\gamma}^p$ is related to the stress actig in the viscoplastic element through a power-law relationship (Equation (12)):

$$\dot{\gamma}^p = \left(\frac{\tau}{f_p \hat{\tau} f_{ep}}\right)^m \tag{12}$$

where $\hat{\tau}$ is the shear flow resistance, m is the shear flow exponent, f_p is the pressure dependence of the flow element given by (Equation (13)):

$$f_p = r\tau_{\frac{t}{c}} + (1 - r) \tag{13}$$

being (Equation (14))

$$r = \begin{cases} 1 & \text{if} \quad \dfrac{\mathrm{tr}(T)}{T_M} \leq -1 \\ 0 & \text{if} \quad \dfrac{\mathrm{tr}(T)}{T_M} \geq 1 \\ \dfrac{\mathrm{tr}(T)}{2T_M} & \text{if} \quad -1 < \dfrac{\mathrm{tr}(T)}{T_M} < 1 \end{cases} \tag{14}$$

with T_M, the von Mises stress. f_{ep} is a function that captures strain softening after yield as (Equation (15)):

$$f_{ep} = f_f + (1 - f_f)\exp\left[\frac{-\epsilon_p}{\hat{\varepsilon}}\right] \tag{15}$$

where ϵ_p is the applied effective Mises plastic strain, f_f is the final value of $\hat{\tau}$ after softening and $\hat{\varepsilon}$ is a characteristic transition strain.

From these relationships, nine constitutive parameters emerge: E, ν, $\hat{\tau}$, m, $\hat{\varepsilon}$, f_f, μ, λ_{lock} and $\tau_{t/c}$. Therefore, the model is here called EVP-9 model (nine-parameter elastic-viscoplastic model).

2.4. Calibration of EVP-9 constitutive model for RTM6

E and ν were taken directly from the material technical data sheet of RTM6 (HexFlow® RTM6, Hexcel) while $\tau_{t/c}$ was calculated from reported data in [35]. The rest of the constitutive parameters ($\hat{\tau}$, m, $\hat{\varepsilon}$, f_f, μ and λ_{lock}) were calibrated with the aid of a commercial application that allows semi-automatic extraction of material parameters from experimental data (MCalibration®, PolymerFEM.com). A three-step procedure was developed using RTM6 uniaxial tensile and compression experimental data reported in the literature for different strain rates by Morelle *et al*. [30]. Parameters were first initialized and subsequently refined using different portions of uniaxial stress-strain curves. μ and λ_{lock} parameters were determined from the last portion of stress-strain curves measured at low strain rates while $\hat{\tau}$, m, $\hat{\varepsilon}$, and f_f parameters were adjusted from yielding and strain-softening portions of uniaxial stress-strain curves at different strain rates.

2.5. Finite element modeling of Berkovich indentation

An axisymmetric 2D model was implemented in a finite element analyzer (Abaqus 6.14/Standard, Dassault Systemes Simulia Corp., USA) to simulate the response of RTM6 specimen to Berkovich indentation at different constant loading strain rates. The indenter was modeled as a rigid cone with an equivalent apical angle of 70.3° that has the same projected area to penetration depth ratio as the Berkovich tip. This is a common approach to accommodate the actual triangular pyramidal geometry in an axisymmetric configuration [20, 21, 36–38]. RTM6 sample behavior was described by the calibrated EVP-9 constitutive model. The constitutive model was implemented in a UMAT using the PolyUMod software [23]. The contact between the indenter and sample was considered frictionless, and no interpenetration was admitted. The RTM6 sample was modeled as a rectangle, which was set large enough to avoid boundary effects. Four nodded quadrilateral elements were used to consider shear stresses. As shown in Figure 2, very fine meshes of a similar size were created at the indenter edge-tip and the contact point of the specimen with node-on-node first touch, while a coarse mesh size was created in the boundary area where no deformation was computed aiming to reduce computational time. Both

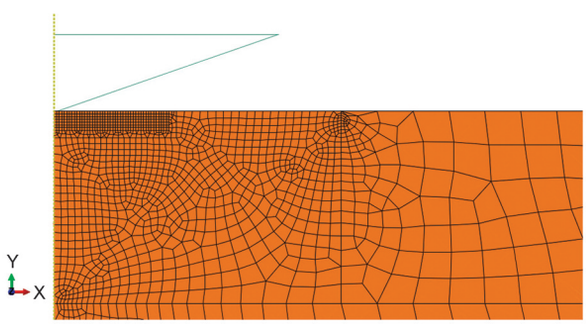

Figure 2. Finite element mesh used in simulations of Berkovich indentation.

specimen rectangle and element sizes were varied systematically until simulated *P–h* curves resulted independently of them.

3. Results and discussion

3.1. Physical nano-indentation experiments

3.1.1. Effect of maximum load and load-hold time

Nano-indentation response of RTM6 sample was first explored by varying P_{max} and thold in the experiments. Some of the results are shown in Figures 3a and 3b. As expected, the loading segment of the *P–h* curves exhibits a parabolic shape. During the load-hold period, the tip displacement increases due to the viscous creep phenomenon. On unloading, viscoelastic displacements are recovered, leaving an indentation imprint on the sample surface (the indenter losses contact with the sample surface at large penetration displacements). Experiments display very good reproducibility as judged by the overlapping of the loading portions of *P–h* curves obtained at different P_{max}.

As P_{max} increases keeping constant *CSR*, thold and tunload, the maximum tip penetration depth, the creep displacement during the load-hold stage, and the residual penetration depth increase (Figure 3a). In addition, reducing the load-hold time while keeping constant *CSR*, P_{max} and tunload conditions cause a decrease in the maximum tip penetration depth due to a smaller creep displacement (Figure 3b).

S, E_r and *H* values from the Oliver and Pharr approach are listed in Table 1, together with W_p values. *H* does not exhibit the marked increasing trend expected with decreasing indentation depth (*i.e.*, decreasing P_{max}) from indentation size effects; they appear almost constant. As P_{max} increases, *S* and W_p markedly increase, while E_r is slightly enhanced. The influence of thold on indentation response due to the creep effect is also reflected in the calculated parameters, as it is usually observed in polymers [8, 10–12]. For the highest P_{max} condition, *S* and E_r decrease while *H* and W_p increase with decreasing t_{hold} from 10 to 5 s.

The highest P_{max} and thold values assayed during exploratory tests were selected to study the effect of *CSR* on the indentation response of RTM6 since viscous effects seem to be more evident.

3.1.2. Effect of *CSR* on RTM6 nanoindentation response

For each *CSR* condition, an average load-time (*P–t*) curve was calculated from the 16 replication tests.

Table 1. Contact stiffness, reduced elastic modulus, indentation hardness, and plastic work values determined from *P–h* curves measured in exploratory experiments at $CSR = 0.25\ s^{-1}$.

P_{max} [μN]		1500	3000	4500	6000	6000
t_{hold} [s]		10	10	10	10	5
S	[μN/nm]	9.85±0.10	14.73±0.07	18.23±0.07	21.80±0.05	21.06±0.06
E_r	[GPa]	3.61±0.04	3.77±0.02	3.82±0.03	4.02±0.02	3.92±0.02
H	[MPa]	256.13±3.43	247.55±1.10	249.43±3.33	260.55±4.02	265.66±2.52
W_p	[nJ]	0.194±0.003	0.550±0.004	0.991±0.011	1.441±0.020	1.393±0.010

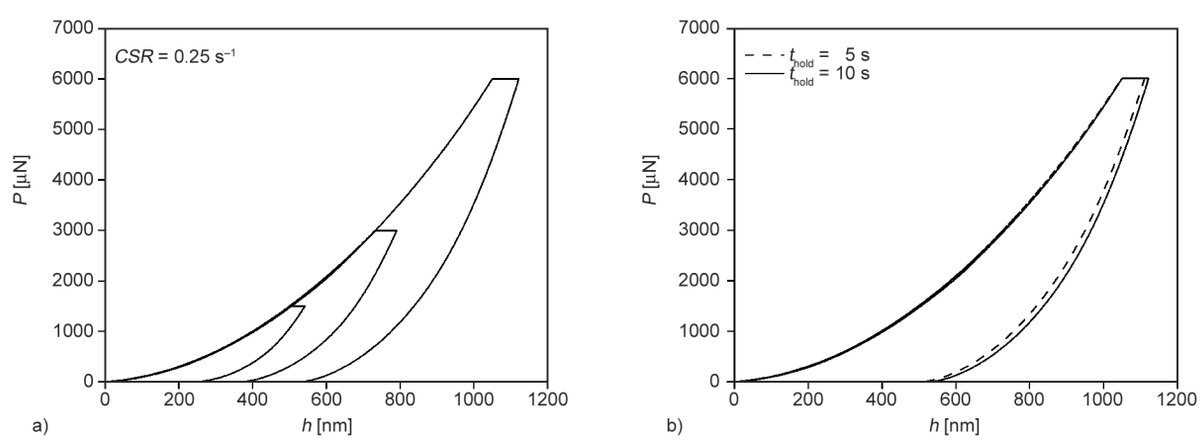

Figure 3. Typical *P–h* curves obtained in exploratory physical nano-indentation experiments at $CSR = 0.25\ s^{-1}$: a) four different maximum applied loads and b) two different load-hold times.

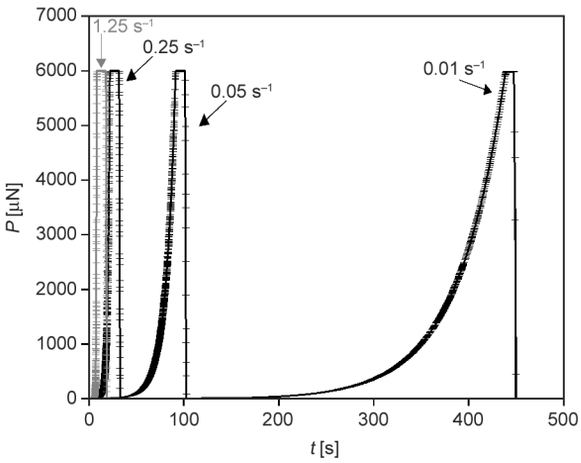

Figure 4. Average load-time curves obtained in physical nano-indentation experiments at different *CSR* conditions. In all cases, t_{hold} = 10 s and P_{max} = 6000 μN.

In Figure 4, the average *P–t* curves obtained for the different *CSR* conditions are shown together with the standard error for time data. *P–t* curves resulted in highly reproducible as judged by the small standard error bars.

The shape of the loading part of *P–t* curves is consistent with the applied exponential loading function (Equation (2)), and the time required to complete the indentation experiments increases with decreasing *CSR*.

The effect of *CSR* on RTM6 indentation response is depicted in Figure 5, in which representative indentation *P–h* curves (Figure 5a) and creep displacement growth during the load-hold period (Figure 5b) are compared. The indentation response is affected by the loading history. On loading, *P–h* curves shift upwards with increasing *CSR*, indicating that the sample resistance to indentation gradually increases with *CSR*. As well, the penetration displacement at which the maximum load is reached decreases, and the maximum displacement attained in the whole experiment increases. Also, the maximum displacement attained at the end of the load-hold period becomes larger at higher *CSR*. This means that RTM6 is more susceptible to creep during the load-hold period at higher *CSR* (*i.e.*, shorter loading times) since creep deformation is not fully exhausted during the loading stage.

Equivalent results have already been reported in the literature for other polymeric materials and testing conditions, confirming the greater creep susceptibility of polymers with increasing indentation loading rate [11, 12, 39, 40]. Shen *et al*. [39] explored the strain rate effect (0.02–2 s^{-1}) on the indentation response of neat polyamide 66 (PA66) and clay nanocomposites and found that creep displacement at the load-hold stage significantly increases with increasing strain rate. Jin *et al*. [40] investigated the effects of indentation loading rate conditions (0.0375–3 mN/s) on the PMMA sample and observed a pronounced decrease in displacement during loading and a marked increase in creep displacement as the indentation rate increases up to 1 mN/s. Yasin *et al*. [11] investigated the effect of strain rate (0.02–1 s^{-1}) upon the indentation response of low density polyethylene (LDPE) in CSM mode and also observed an increase in creep displacement with increasing strain rate. Similar studies carried out by Iqbal *et al*. [12] on ultrahigh molecular weight polyethylene (UHMWPE) at varying strain rates (0.02–2 s^{-1}) showed that *P–h* curves shift towards lower indentation depths along with an increase in peak load by increasing the indentation strain rate.

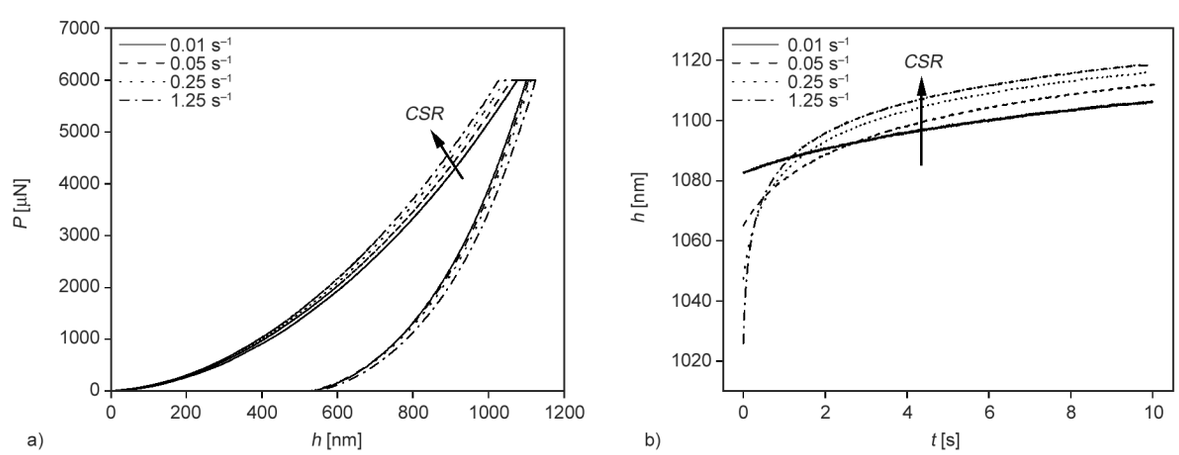

Figure 5. Indentation response of RTM6 sample at different *CSR* conditions: a) representative *P–h* curves; b) representative *h–t* curves in the load-hold period.

P–h curves obtained at different *CSR* were analyzed following the Oliver-Pharr approach; the determined parameters are reported in Table 2. The contact stiffness appeared to be unaffected by *CSR*, probably due to the fast-unloading rate and the load-hold period used in the experiments that minimized the influence of creep phenomena on the unloading curve [9]. E_r and H values show decreasing trends with increasing loading strain rate, which do not correlate with the conventional mechanical properties' dependence on strain rate. Elastic modulus must show practically no variation with strain rate, while hardness, which is proportional to yield stress, should increase with increasing strain rate in agreement with the Eyring equation [41]. According to Oliver-Pharr method equations [5], surface mechanical properties depend on the contact area (Equations (4) and (5)). Ac increases with contact penetration depth (Equations (6)), which in turn increases with maximum penetration depth (Equations (3)). As it was shown in Figure 4, h_{max} increases with increasing *CSR*. Therefore, the source of the observed trend in E_r and H values with *CSR* arises from A_c estimation. Because of the viscous nature of RTM6 behavior, the Oliver-Pharr approach yields rather unreliable nanomechanical properties and a dependence on loading strain rate that differs from that of the conventional bulk mechanical properties of RTM6 epoxy polymer [30, 35].

Tang and Ngan [10] proposed adapting the Oliver-Pharr method to viscoelastic materials discounting the creep contribution to the maximum displacement in contact depth estimation. This procedure will yield an increasing trend in E_r and H values with an increasing loading strain rate. This method is only a phenological approximation [10] that does not describe the inherent polymer behavior dependence with strain rate.

Plastic work values are also shown in Table 2. W_p increase as *CSR* increases, indicating that RTM6 behaves more plastic at higher strain rates. Shen *et al*. [39] explain this phenomenon as follows: as the indentation strain rate is faster, there is less time for the polymer chains to recover elastically after the external load removes, leading to plastic deformation left in the sample.

3.2. Simulated indentation response

To interpret the effect of strain rate on the indentation response of RTM6 epoxy resin, the sharp indentation problem of an elastic-viscoplastic material was numerically simulated using the FE model described in Section 2.5. The constitutive parameters of the EVP-9 model were first determined, as described in Section 2.4. Then, the FE model was used in forward analysis to simulate indentation *P–h* curves for the same *CSR*, P_{max}, t_{hold} and tunload conditions than those used in physical nano-indentation experiments. A sensitivity analysis of *P–h* curve to EVP-9 model parameters was carried out complementary.

3.2.1. EVP-9 constitutive model parameters of RTM6

Two relevant studies specifically dedicated to the deformation characterization of RTM6 epoxy resin under different strain rates and loading conditions have been published [30, 35]. Morelle *et al*. [30] experimentally studied the non-linear deformation properties of RTM6 as a function of strain rate (in the quasi-static range) and temperature under various stress states involving uniaxial tension, notched tension, uniaxial compression, torsion, and shear configurations. They show that RTM6 exhibits a classical rate, temperature, and hydrostatic pressure-dependent behavior, with yielding followed by strain softening and re-hardening at larger strains and important viscoplastic effects [30]. Gerlach *et al*. [35] studied the mechanical behavior of RTM6 epoxy resin at strain rates ranging from 10^{-4} to 10^{4} s^{-1}. Their investigations evidence that the material yield

Table 2. Contact stiffness, reduced elastic modulus, indentation hardness, and plastic work values determined from measured *P–h* curves at different *CSR* conditions.

		CSR **[s^{-1}]**			
		0.01	**0.05**	**0.25**	**1.25**
S	[μN/nm]	21.68±0.07	21.62±0.08	21.80±0.05	21.51±0.57
E_r	[GPa]	4.06±0.05	4.03±0.03	4.02±0.02	3.94±0.09
H	[MPa]	267.17±6.72	263.56±3.73	260.55±4.02	257.19±3.46
W_p	[nJ]	1.225±0.012	1.338±0.008	1.441±0.020	1.604±0.010

stress increases with increasing strain rate and shows a strong hydrostatic stress sensitivity [35].

The advantage of the EVP-9 constitutive model over more complex ones relies on the fact that every constitutive parameter is directly related to a specific characteristic of the stress-strain behavior. E and ν are the elastic properties, $\hat{\tau}$ is related to the elastic limit or material yields stress, m and $\tau_{t/c}$ are respectively linked with yield stress-strain rate and hydrostatic pressure dependencies, $\hat{\varepsilon}$ and f_f are associated with post-yielding softening behavior, while μ and λ_{lock} are linked with strain hardening. This feature allowed the staggered identification of each model parameter from specific portions of the stress-strain curves. The determined constitutive parameters for RTM6 epoxy resin are listed in Table 3.

In Figure 6, the experimental data reported in [30] for RTM6 under uniaxial compression at different constant displacement rates (*i.e.*, different constant engineering strain rates) are compared with the ones predicted by the calibrated EVP-9 model. The predicted uniaxial compression stress-strain (σ–ε) curves were obtained using the MCalibration application. Overall, good agreement between experimental and predicted σ–ε curves is observed except for the highly non-linear behavior that anticipates the extrinsic yield point. EVP-9 model slightly overestimates the magnitude of the yield peak, but it can capture the strain rate dependence of the compressive yield stress. The model reproduces the elastic as well as the post-yield strain-softening and strain-hardening behaviors with accuracy. The discrepancy in the shape of the σ–ε curve that precedes the yield peak is inherent to this kind of model [42]. In fact, Ames and Anand [16] commented that even if these types of phenomenological models capture the large deformation elastic-viscoplastic response of polymers quite well, they are less successful in accounting for the creep response at stress levels below those causing 'macro-yield'. A more powerful constitutive model that well describes the micro-indentation response of PMMA has been proposed by them [22]. However, such a model would result impossible to adopt here since it requires the knowledge of more than thirty constitutive parameters, which are currently unknown for RTM6.

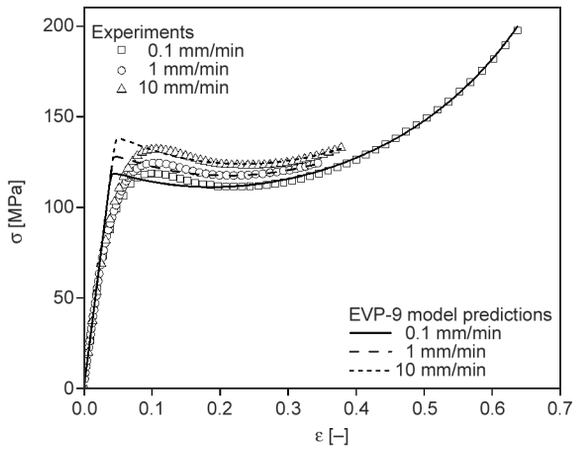

Figure 6. Comparison of experimental uniaxial compression stress-strain curves for RTM6 at different displacement rates [30] with EVP-9 constitutive model predictions.

3.2.2. Effect of *CSR* on simulated RTM6 indentation response

Simulated RTM6 indentation P–h curves at the different *CSR* conditions are presented in Figure 7a. The portion of P–h around the load-hold step is zoomed in to gain clarity in Figure 7b.

Simulated P–h curves exhibited very similar characteristics to those of physically measured P–h curves (Figure 5). They display appreciable creep displacement growth at maximum indentation load. As the indentation strain rate increases, the penetration depth achieved at the end of the loading step decreases. As well, the maximum penetration depth attained at the end of the load-hold stage increases (Figure 7b). Moreover, the unloading P–h curve appears to be unaffected by the previous loading strain rate.

The dashpot element in network A (Figure 1) and the plastic strain rate power law relationship of the stress acting in the viscoplastic element of the EVP-9 model (Equation (12)), which depends on m, $\hat{\varepsilon}$, $\hat{\tau}$ and f_f parameters were quite successful in reproducing the loading strain rate dependence of the RTM6 indentation response observed in the studied *CSR* range in physical experiments (Figure 5).

In Figure 8, physically measured and simulated indentation curves are compared for each *CSR* condition. A quite good correlation is found between physically measured data and numerical simulations,

Table 3. EVP-9 constitutive parameters of RTM-6 epoxy resin used in numerical simulations.

Parameter	E [GPa]	ν	$\hat{\tau}$ [MPa]	m	$\hat{\varepsilon}$	f_f	μ [MPa]	λ_{lock}	$\tau_{t/c}$
Value	2.89	0.4	121.99	29.9	0.25	0.12	0.4	1.36	0.66

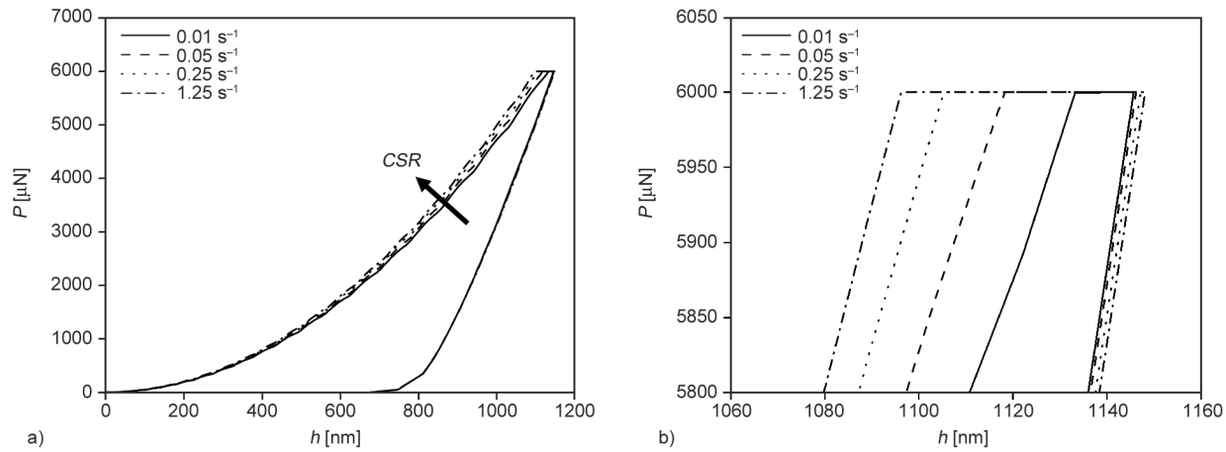

Figure 7. Simulated indentation response of RTM6 at different *CSR* conditions: a) *P–h* curves; b) zoom portion of *P–h* curves around the load-hold period.

despite the simplicity of the EVP-9 constitutive model, the fact that EVP-9 model parameters were calibrated using macroscale experimental data published elsewhere [30, 35], the idealization of the Berkovich indentation problem in the FE model and, the experimental errors. Overall, in all *CSR* conditions, simulated *P–h* curves are slightly shifted to larger displacements. The model predicted *P–h* curve is less steep during loading, tip displacement at the load hold is smaller, and residual penetration depths are larger than those registered in physical measurements. Discrepancies in the loading curve may be partially attributed to the ideally sharp indenter adopted in FEM simulations since actual Berkovich tips

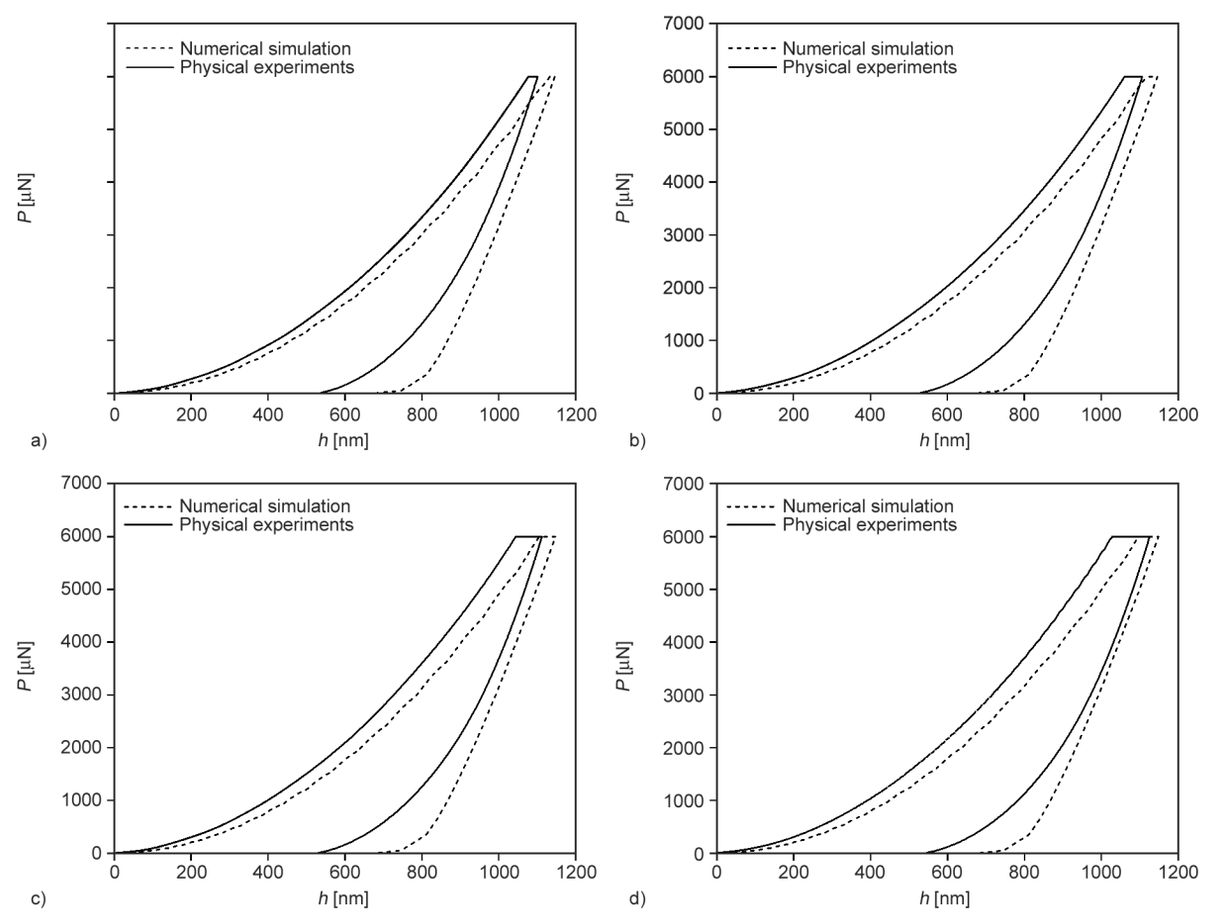

Figure 8. Comparison of *P–h* curves obtained in RTM6 nano-indentation experiments and numerical simulations for different *CSR*: a) 0.01 s^{-1}; b) 0.05 s^{-1}; c) 0.25 s^{-1}; d) 1.25 s^{-1}.

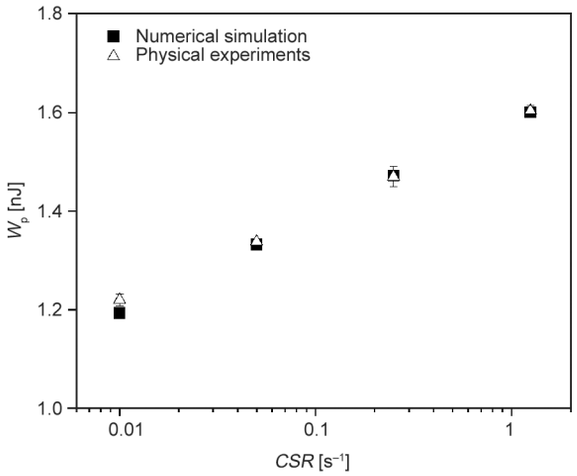

Figure 9. Comparison of plastic work values determined from measured and simulated *P–h* curves for different *CSR*.

are always blunted. It has been shown that the steepness of the *P–h* curves grows with the tip roundness [43]. FEM experiments did not consider the actual tip geometry because its roundness is unknown.

In Figure 9, plastic work values determined from simulated *P–h* curves are plotted as a function of *CSR*. This plot confirms that plastic work increases as the strain rate increases for an elastic viscoplastic material. Despite model assumptions and problem idealization, W_p values obtained from simulations overlap those obtained from physical nano-indentations.

From the comparison of *P–h* curves shown in Figures 5a and 7), it can be stated that the FE model is able to capture the effect of load loading strain rate on creep displacement growth at the load-hold pveriod even if its results are slightly underestimated. However, the dependence of the inelastic deformation energy on the loading strain rate is excellently reproduced (Figure 9). As well, contact stiffness values (*S*) determined from simulated curves are independent of *CSR* in agreement with those obtained from physically measured *P–h* curves (Table 2).

Finally, to analyze the influence of EVP-9 parameter values on Berkovich indentation response, several simulations were performed using the FE model and

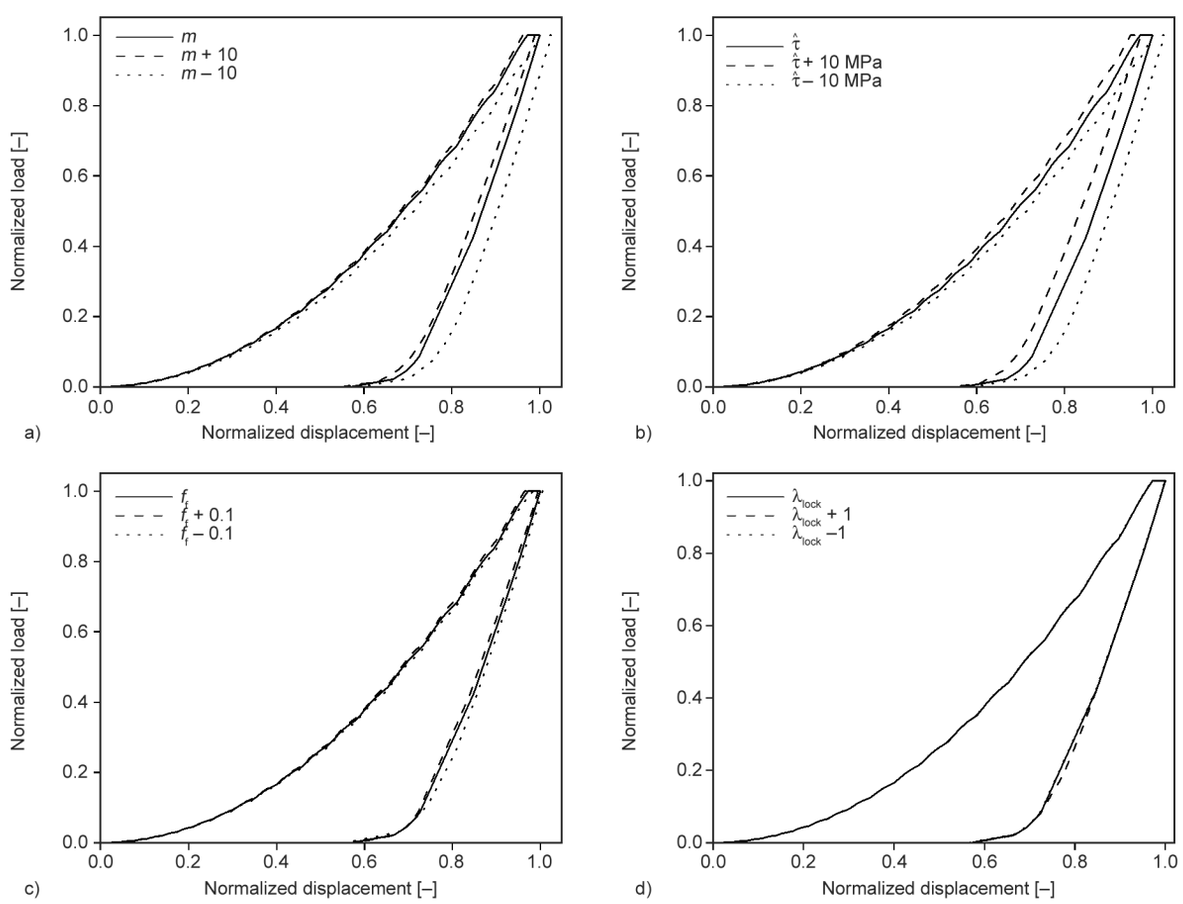

Figure 10. Influence of selected EVP-9 model parameters on simulated Berkovich indentation responses at *CSR* = 0.25 s^{-1}: a) *m*; b) $\hat{\tau}$; c) f_f; d) λ_{lock}. Load was normalized by P_{max} (6000 μN) and displacement by the maximum tip displacement for the base case parameter.

making one EVP-9 model parameter vary while keeping the other constitutive parameters constant. Representative results of this sensitivity analysis are shown in Figure 10. It was found that Berkovich indentation response is mainly influenced by E, ν, m and $\hat{\tau}$, slightly affected by $\hat{\varepsilon}$ and f_f and practically unaffected by μ and λ_{lock} parameters. The latter means that parameters associated with strain-hardening behavior could not be easily and unambiguously identified from Berkovich nano-indentation data.

4. Conclusions

Indentation strain rate-dependent deformation behavior of an aerospace-grade epoxy resin was experimentally explored by nano-indentation tests conducted at constant loading strain rates ranging from 0.01 to 1.25 s^{-1}. It was appreciated that the maximum displacement achieved at the end of the load-hold period was larger at higher indentation strain rates. This means that the epoxy sample is more susceptible to creep during the dwell period at higher strain rates and so that creep deformation is unable to fully develop during the indentation loading stage. Plastic work also increases with increasing loading strain rate.

Indentation simulation experiments considering a nine-parameter elastic-viscoplastic constitutive model which captures time-dependent behavior, strain softening and hardening and uneven yielding under multiaxial stress states were able to reproduce reasonably well the indentation response of the RTM6 sample and to predict almost perfectly the plastic work values for the studied constant loading strain rates.

Acknowledgements

This work was financially supported by the National Research Agency of Argentina, ANCyPT, Budget PICT-2016-0302. Authors gratefully acknowledge the help of Eng. Bernardo Daga in physical indentation experiments.

References

[1] Moosburger-Will J., Greisel M., Horn S.: Physical aging of partially crosslinked RTM6 epoxy resin. Journal of Applied Polymer Science, **131**, 41121 (2014). https://doi.org/10.1002/app.41121

[2] Moosburger-Will J., Greisel M., Sause M. G. R., Horny R., Horn S.: Influence of partial cross-linking degree on basic physical properties of RTM6 epoxy resin. Journal of Applied Polymer Science, **130**, 4338–4346 (2013). https://doi.org/10.1002/app.39722

[3] Passilly B., Delannoy R.: Characterization of the ageing of an epoxy resin using high temperature nanoindentation. Matériaux & Techniques, **107**, 206 (2019). https://doi.org/10.1051/mattech/2019004

[4] Frontini P., Lotfian S., Monclús M. A., Molina-Aldareguia J. M.: High temperature nanoindentation response of RTM6 epoxy resin at different strain rates. Experimental Mechanics, **55**, 851–862 (2015). https://doi.org/10.1007/s11340-015-9985-4

[5] Oliver W. C., Pharr G. M.: An improved technique for determining hardness and elastic modulus using load and displacement sensing indentation experiments. Journal of Materials Research, **7**, 1564–1583 (1992). https://doi.org/10.1557/JMR.1992.1564

[6] Tranchida D., Piccarolo S., Loos J., Alexeev A.: Mechanical characterization of polymers on a nanometer scale through nanoindentation. A study on pile-up and viscoelasticity. Macromolecules, **40**, 1259–1267 (2007). https://doi.org/10.1021/ma062140k

[7] Kranenburg J. M., Tweedie C. A., van Vliet K. J., Schuber U. S.: Challenges and progress in high-throughput screening of polymer mechanical properties by indentation. Advanced Materials, **21**, 3551–3561 (2009). https://doi.org/10.1002/adma.200803538

[8] Hardiman M., Vaughan T. J., McCarthy C. T.: The effects of pile-up, viscoelasticity and hydrostatic stress on polymer matrix nanoindentation. Polymer Testing, **52**, 157–166 (2016). https://doi.org/10.1016/j.polymertesting.2016.04.003

[9] Feng G., Ngan A. H. W.: Effects of creep and thermal drift on modulus measurement using depth-sensing indentation. Journal of Material Research, **17**, 660–668 (2002). https://doi.org/10.1557/JMR.2002.0094

[10] Tang B., Ngan A. H. W.: Accurate measurement of tip-sample contact size during nanoindentation of viscoelastic materials. Journal of Materials Research, **18**, 1141–1148 (2003). https://doi.org/10.1557/JMR.2003.0156

[11] Yasin S., Shakeel A., Iqbal T., Ahmad F., Mehmood H., Luckham P. F., Ullah N.: Effect of experimental conditions on nano-indentation response of low density polyethylene (LDPE). Journal of Macromolecular Science Part A: Pure and Applied Chemistry **56**, 640–647 (2019). https://doi.org/10.1080/10601325.2019.1593791

[12] Iqbal T., Camargo S. S., Yasin S., Farooq U., Shakeel A.: Nano-indentation response of ultrahigh molecular weight polyethylene (UHMWPE): A detailed analysis. Polymers, **12**, 795–809 (2020). https://doi.org/10.3390/polym12040795

[13] Frontini P.: Nanoindentation: An emerging technique for polymer surface mechanical characterization. Express Polymer Letters, **1**, 640 (2007). https://doi.org/10.3144/expresspolymlett.2007.87

[14] Hasan O. A., Boyce M. C.: A constitutive model for the nonlinear viscoelastic viscoplastic behavior of glassy polymers. Polymer Engineering and Science, **35**, 331–344 (1995). https://doi.org/10.1002/pen.760350407

[15] Anand L., Gurtin M. E.: A theory of amorphous solids undergoing large deformations, with application to polymeric glasses. Journal of the Mechanics and Physics of Solids, **40**, 1465–1487 (2003). https://doi.org/10.1016/S0020-7683(02)00651-0

[16] Ames N., Anand L.: A theory of amorphous polymeric solids undergoing large deformations: Application to micro-indentation of poly(methyl methacrylate). Department of Mechanical Engineering Massachusetts Institute of Technology, Cambridge (2004).

[17] Bergström J. S., Rimnac C. M., Kurtz S. M.: Prediction of multiaxial mechanical behavior for conventional and highly crosslinked UHMWPE using a hybrid constitutive model. Biomaterials, **24**, 1365–1380 (2003). https://doi.org/10.1016/S0142-9612(02)00514-8

[18] Bergström J., Bischoff J.: An advanced thermo-mechanical constitutive model for UHMWPE. International Journal of Structural Changes in Solids, **2**, 31–39 (2010).

[19] Govaert L. E., Timmermans P. H. M., Brekelmans W. A. M.: The influence of intrinsic strain softening on strain localization in polycarbonate: Modeling and experimental validation. Journal of Engineering Materials and Technology, **122**, 177–185 (2000). https://doi.org/10.1115/1.482784

[20] Rueda-Ruiz M., Beake D. B., Molina-Aldareguia J. M.: Determination of rate-dependent properties in cohesive frictional materials by instrumented indentation. JOM, **74**, 2206–2219 (2022). https://doi.org/10.1007/s11837-022-05268-2

[21] van Breemen L. C. A., Engels T. A. P., Pelletier C. G. N., Govaert L. E., den Toonder J. M. J.: Numerical simulation of flat-tip micro-indentation of glassy polymers: Influence of loading speed and thermodynamic state. Philosophical Magazine, **89**, 677–696 (2009). https://doi.org/10.1080/14786430802441188

[22] Anand L., Ames N. M.: On modeling the micro-indentation response of an amorphous polymer. International Journal of Plasticity, **22**, 1123–1170 (2006). https://doi.org/10.1016/j.ijplas.2005.07.006

[23] PolyUMod – A library of advanced user materials. Veryst Engineering, Needham, Massachusetts (2012).

[24] Jayachandran R., Boyce M. C., Montagut E., Argon A. S.: Thermomechanical analysis of indentation behavior of thin PMMA coatings. Journal of Computer-Aided Materials Design, **2**, 23–48 (1995). https://doi.org/10.1007/BF00701679

[25] Bergström J. S., Boyce M. C.: Constitutive modeling of the large strain time-dependent behavior of elastomers. Journal of the Mechanics and Physics of Solids, **46**, 931–954 (1998). https://doi.org/10.1016/S0022-5096(97)00075-6

[26] Mulliken A. D., Boyce M. C.: Mechanics of the rate-dependent elastic–plastic deformation of glassy polymers from low to high strain rates. International Journal of Solids and Structures, **43**, 1331–1356 (2006). https://doi.org/10.1016/j.ijsolstr.2005.04.016

[27] Vieira A. C., Guedes R. M., Tita V.: Constitutive modeling of biodegradable polymers: Hydrolytic degradation and time-dependent behavior. International Journal of Solids and Structures, **51**, 1164–1174 (2014). https://doi.org/10.1016/j.ijsolstr.2013.12.010

[28] Torres J. P., Frontini P. M.: Mechanics of polycarbonate in biaxial impact loading. International Journal of Solids and Structures, **85–86**, 125–133 (2016). https://doi.org/10.1016/j.ijsolstr.2016.02.010

[29] Fu G., Sun F., Huo D., Shyha I., Sun F., Fang C.: FE-simulation of machining processes of epoxy with Mulliken Boyce model. Journal of Manufacturing Processes, **71**, 134–146 (2021). https://doi.org/10.1016/j.jmapro.2021.09.026

[30] Morelle X., Chevalier J., Bailly C., Pardoen T., Lani F.: Mechanical characterization and modeling of the deformation and failure of the highly crosslinked RTM6 epoxy resin. Mechanics of Time-Dependent Materials, **21**, 419–454 (2017). https://doi.org/10.1007/s11043-016-9336-6

[31] Fisher-Cripps C.: Nanoindentation. Springer, New York (2004).

[32] Cheng Y-T., Cheng C-M.: Scaling, dimensional analysis, and indentation measurements. Materials Science and Engineering R: Reports, **44**, 91–149 (2004). https://doi.org/10.1016/j.mser.2004.05.001

[33] Lucas B. N., Oliver W. C., Pharr G. M., Loubet J. L.: Time dependent deformation during indentation testing. MRS Online Proceedings Library, **436**, 233–238 (1997). https://doi.org/10.1557/PROC-436-233

[34] Alisafaei F., Han C-S., Lakhera N.: Characterization of indentation size effects in epoxy. Polymer Testing, **40**, 70–78 (2014). https://doi.org/10.1016/j.polymertesting.2014.08.012

[35] Gerlach R., Siviour C. R., Petrinic N., Wiegand J.: Experimental characterisation and constitutive modelling of RTM-6 resin under impact loading. Polymer, **49**, 2728–2737 (2008). https://doi.org/10.1016/j.polymer.2008.04.018

[36] Bucaille J. L., Felder E., Hochstetter G.: Identification of the viscoplastic behavior of a polycarbonate based on experiments and numerical modeling of the nano-indentation test. Journal of Materials Science, **37**, 3999–4011 (2002). https://doi.org/10.1023/A:1019644630927

[37] Hyun H. C., Kim M., Lee J. H., Lee H.: A dual conical indentation technique based on FEA solutions for property evaluation. Mechanics of Materials, **43**, 313–331 (2011). https://doi.org/10.1016/j.mechmat.2011.03.003

[38] Karimzadeh A., Ayatollahi M. R., Alizadeh M.: Finite element simulation of nano-indentation experiment on aluminum 1100. Computational Materials Science, **81**, 595–600 (2014). https://doi.org/10.1016/j.commatsci.2013.09.019

[39] Shen L., Phang I. Y., Liu T., Zeng K.: Nanoindentation and morphological studies on nylon 66/organoclay nanocomposites. II. Effect of strain rate. Polymer, **45**, 8221–8229 (2004). https://doi.org/10.1016/j.polymer.2004.09.062

[40] Jin T., Niu X., Xiao G., Wang Z., Zhou Z., Yuan G., Shu X.: Effects of experimental variables on PMMA nano-indentation measurements. Polymer Testing, **41**, 1–6 (2015). https://doi.org/10.1016/j.polymertesting.2014.09.015

[41] Kontou E.: Viscoplastic deformation of an epoxy resin at elevated temperatures. Journal of Applied Polymer Science, **101**, 2027–2033 (2006). https://doi.org/10.1002/app.23768

[42] Richeton J., Ahzi S., Vecchio K. S., Jiang F. C., Makradi A.: Modeling and validation of the large deformation inelastic response of amorphous polymers over a wide range of temperatures and strain rates. International Journal of Solids and Structures, **44**, 7938–7954 (2007). https://doi.org/10.1016/j.ijsolstr.2007.05.018

[43] Kovář J., Fuis V., Tomáštík J.: Influencing the indentation curves by the bluntness of the Berkovich indenter at the FEM modelling. Acta Polytechnica, **27**, 131–135 (2020). https://doi.org/10.14311/APP.2020.27.0131